Materials Characterization 194 (2022) 112405

Contents lists available at ScienceDirect

Materials Characterization

journal homepage: www.elsevier.com/locate/matchar

Crystallographic aspects of 17–4 PH martensitic steel produced by laser-powder bed fusion

Igor Vysotskiy, Sergey Malopheyev, Ivan Zuiko, Sergey Mironov *, Rustam Kaibyshev

Belgorod National Research University, Pobeda 85, Belgorod 308015, Russia

ARTICLE INFO

Keywords:
Additive manufacturing
Martensitic steel
Electron backscatter diffraction (EBSD)
Phase transformation
Microstructure
Texture

ABSTRACT

Microstructural evolution during laser-powder bed fusion of 17–4 PH martensitic steel was studied. Particular emphasis was paid to the crystallographic aspects of this process. The crystallization of δ-ferrite from the liquid phase was shown to be governed by an epitaxial mechanism which gave rise to the solidification ⟨100⟩ − fiber texture. The austenitic phase preferentially nucleated at the ferrite grain boundaries, while the subsequent migration of phase boundaries was accompanied by extensive annealing twinning. Remarkably, the grain-boundary austenite was related to both adjacent ferrite grains via the Nishiyama-Wasserman orientation relationship. The multiple crystallographic variants associated with the phase transformation and annealing twinning resulted in a comparatively weak ⟨110⟩ + <100> − fiber texture in austenite. The subsequent austenite → martensite phase transformation was governed by the mixed orientation relationship, which included both the Nishiyama-Wasserman and Kurdjumov-Sachs ones. The nearly-random texture in martensite suggested no essential variant selection during the phase transformation.

1. Introduction

Precipitation-hardened (PH) martensitic steels offer a promising balance of high strength and good corrosion resistance at service properties below 300 °C. Accordingly, these materials are widely used for nuclear, aerospace, marine, and chemical applications. Unfortunately, the relatively poor workability of these steels may cause difficulties in the fabrication of complex-shaped products. Hence, additive manufacturing (AM) is sometimes considered a potential game changer in this area.

Among various AM techniques, laser-powder bed fusion (LPBF) (which is also often referred to as selective laser melting, or SLM) is currently gaining increased attention. This is primarily due to a combination of the following factors: (i) the ability of this approach to process advanced metallic materials (such as steels, titanium, and nickel-based alloys), (ii) almost unlimited design freedom, and (iii) high manufacturing accuracy [1]. Technically, LPBF involves the incremental, layer-by-layer melting and fusion of a metal powder according to the sliced Computer Aided Design (CAD) model in order to create a three-dimensional object. Material melting is achieved by using a laser beam of high energy density that moves in a distinct pattern for each material layer. Due to the extremely short duration of laser pulsing as well as repetitive melting of neighboring material layers, LPBF gives rise to a very complex thermal history. It includes an extremely rapid cooling rate ($\sim 10^6$ s^{-1}), a sharp temperature gradient, and thermal cycling. In turn, this environment results in very specific microstructures within the manufactured products.

Amid various PH martensitic steels, the 17–4 PH grade is currently the most popular for LPBF applications. This is primarily due to the relatively good weldability of this material. LPBF-induced microstructure in this steel is typically a mixture of different phases, such as martensite and austenite [2–9], martensite and δ-ferrite [10], or even δ-ferrite, austenite, and martensite [11–13]. In some cases, however, the development of a single-phase martensite [2,7] or δ-ferrite [12,14,15] has also been reported. The wide range of the possible phase structures is likely associated with the variation of particular LPBF conditions. Specifically, an application of nitrogen shielding during LPBF promotes the formation of the austenitic phase [2,4,16], likely due to the austenite stabilizing effect of nitrogen. The same effect has been observed during the use of water-atomized metallic powder [17]. Moreover, the phase composition also depends on LPBF variables. In particular, an increment in the laser energy density increases the volume fraction of the martensitic phase, while a reduction in the spacing between the successive laser scans (i.e., the hatch distance) promotes the austenite

* Corresponding author.
E-mail address: mironov@bsu.edu.ru (S. Mironov).

https://doi.org/10.1016/j.matchar.2022.112405
Received 1 July 2022; Received in revised form 29 September 2022; Accepted 16 October 2022
Available online 19 October 2022

formation [18]. Furthermore, the phase fraction may also be influenced by the orientation of the building direction and the strategy of the laser scans [19].

Remarkably, no significant variation in alloying elements between the phases has been observed [20]. This effect has been attributed to the extremely high cooling rate during LPBF, which presumably minimizes the diffusion-driven redistribution of the elements between the phases [20].

In δ-ferrite, the microstructure is typically dominated by the relatively coarse columnar-shaped grains [4,11,20,21]. These are usually attributed to the crystallization of the ferrite phase from the local molten pools (produced during laser pulsing) and the subsequent growth of the nucleated crystals in the direction of a thermal gradient [11,21]. Typically, the columnar grains exhibit a comparatively complex morphology, thus suggesting the complex character of local thermal fields [4,20,21]. Importantly, the columnar grains often extend over several powder layers [4,11,21] and show the characteristic <100> solidification texture [2,11,12,16,22]. These findings demonstrate the epitaxial mechanism of nucleation of the ferrite phase [20,21].

On the other hand, the austenitic and martensitic phases typically have comparatively fine-grained structures and usually concentrate near the boundaries of the former molten pools [11,21]. In some cases, the nucleation of austenite at the grain boundaries of δ-ferrite was noted [12]. Considering the thermal cycling that is inherent to the LPBF process, it is believed that some portion of austenite may originate from the martensite-to-austenite reversion [8,21].

It is also worth noting that manufactured materials frequently contain manganese- and silicon-rich oxides with nano- to micron-scale sizes [11,23]. The coarse particles are typically arranged between the melt tracks while the nano-scale dispersoids are often situated at the martensite grain boundaries [11,23].

The above studies have provided valuable insight into the LPBF-induced microstructure. It is important to emphasize, however, that relatively little attention has been paid so far to the crystallographic aspects of the manufactured materials. These include the possible orientation relationships between the phases, crystallographic texture in austenite and martensite, and misorientation distributions in all phases. This knowledge gap essentially restricts our fundamental understanding of the processes occurring during LPBF. Moreover, it also limits our ability to predict the service behavior of manufactured products. Therefore, the present work was undertaken to shed some light on this issue.

2. Experimental

To maintain consistency with the results reported in the scientific literature, the program material studied in the present work was a commercial 17–4 PH martensitic steel.[1] The material was supplied by 3D Systems, Inc. in the form of nitrogen-atomized powder.

LPBF was performed using a ProX DMP 200 machine (3D Systems Inc.) under the manufacturer-recommended conditions, i.e., laser power of 240 W, the laser scanning speed of 2500 mm/s, hatch distance of 50 μm, and layer thickness of 30 μm. The material was built vertically while the laser scanning direction was perpendicular to the motion direction of the powder distribution roller. Hence, the LPBF geometry included the laser scanning direction (SD), the roller direction (RD), and the building direction (BD). A cuboidal-shaped sample with dimensions of 10 × 10 × 20 mm^3 (SD × RD × BD) was built in a nitrogen atmosphere using a simple parallel scan strategy with alternating scan directions. The chemical composition of the as-built material was measured by the plasma optical emission spectroscopy and consisted of (wt%) 16.8% Cr, 4.6% Ni, 3.8% Cu, 0.7% Mn, 0.7% Si, 0.2% Nb, 0.07% C, and the balance being Fe. The nitrogen and oxygen contents were determined by the inert gas fusion technique and found to be 0.27 and 0.05 wt%, respectively.

Microstructural observations were conducted primarily using the electron backscatter diffraction (EBSD) technique but also involved energy dispersive spectroscopy (EDS) measurements. The microstructural studies were focused on the longitudinal cross-section (BD x RD plane). The appropriate surface finish was obtained employing conventional metallographic techniques followed by long-term (24-h) vibratory polishing with colloidal silica suspension.

Both EBSD and EDS measurements were performed using an FEI Quanta 600 field-emission-gun scanning electron microscope (SEM) equipped with a TSL OIM™ EBSD-EDS system and operated at an accelerated voltage of 20 kV. In order to investigate the possible variation of microstructure along the building direction, EBSD measurements were carried out in the bottom, central, and top parts of the manufactured sample. To examine microstructure at different length scales, two EBSD maps were acquired in each case, i.e., a low-resolution one (the scan step size of 0.5 μm) and a high-resolution one (the scan step size of 0.2 μm). The total statistics of EBSD measurements are summarized in Table 1. Considering the difficulty of discriminating ferrite from martensite in EBSD, these two phases were indexed as the generic body-centered cubic (BCC) phase; accordingly, the austenite was indexed as the generic face-centered cubic (FCC) phase. To enhance the reliability of EBSD data, the fine grains comprising two or one pixel were automatically "cleaned" from the maps using the standard grain-dilation option of EBSD software. Due to the limited angular accuracy of EBSD, the lower-limit misorientation cut-off of 2^o was applied. Grain size was measured using the equivalent-grain diameter approach, i.e., by measurements of the grain area in the EBSD map and calculating the circle-equivalent diameter [26].

The particular EBSD characteristic, the image-quality (IQ) index (which is also sometimes referred to as pattern quality or band contrast index), was used for microstructural analysis. The IQ index characterizes the sharpness of the Kikuchi bands in a digitized diffraction pattern and serves as a qualitative measure of stored energy.

3. Results and discussion

3.1. Phase partitioning

EBSD measurements revealed no principal difference in microstructure morphology between the bottom, central, and top parts of the manufactured sample. Hence, only a typical EBSD map is shown in Fig. 1a, while the entire set of the acquired maps is given in supplementary Figs. S2-S4. From EBSD data, it is clear that the evolved microstructure was relatively complex and consisted of both BCC and FCC constituents. Moreover, a notable fraction of residual porosity was also worthy of note (black areas in EBSD maps). Importantly, the BCC constituent included two distinctly different components, viz., coarse-

Table 1
Statistics EBSD measurements.

Location	Scan step size, μm	Acquired area, mm^2	Number of pixels	Number of grains*
Bottom	0.5	1.70 × 1.20	9,426,186	241,300
	0.2	0.63 × 0.55	10,005,988	90,716
Center	0.5	1.70 × 1.30	10,211,702	271,651
	0.2	0.45 × 0.45	5,849,050	53,006
Top	0.5	1.70 × 1.35	10,602,759	315,348
	0.2	0.70 × 0.34	6,787,559	92,616

* The grains were defined as local areas in EBSD maps outlined by the grain boundaries with misorientation of 15^o or above.

[1] ThermoCalc predictions of the evolution of the phase composition of 17–4 PH martensitic steel as a function of temperature are shown in supplementary Fig. S1. A detailed analysis of the phase transformations, which occur in this steel at comparatively low heating or cooling rates (≤100 K/s), is provided in Refs. [24, 25].

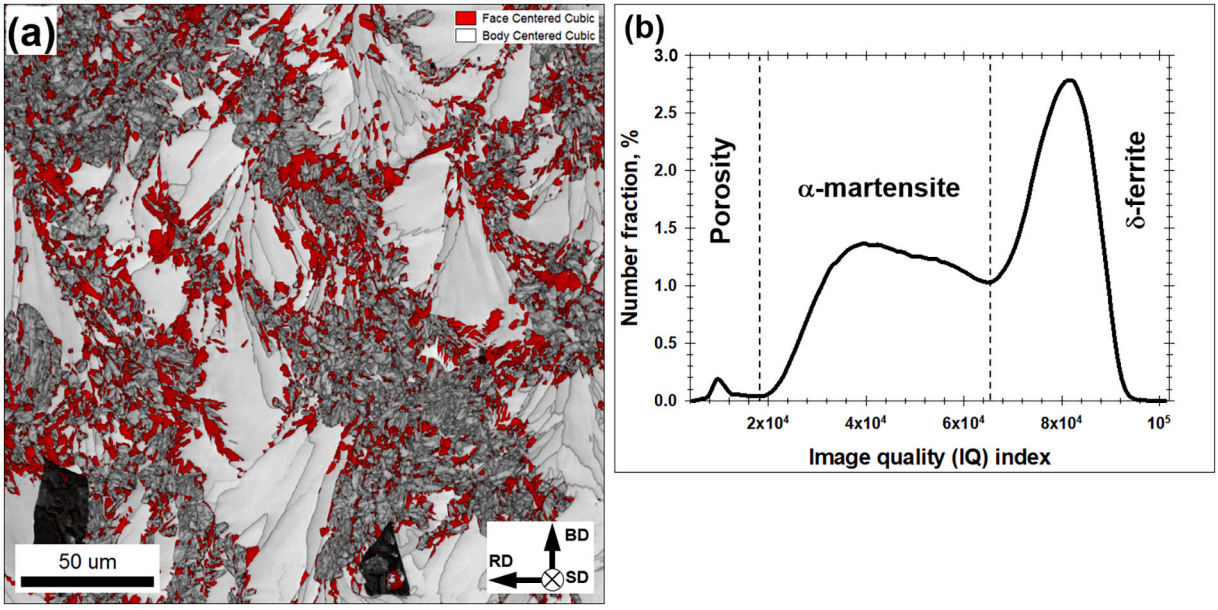

Fig. 1. (a) Selected portion of EBSD image-quality (IQ) map with overlaid phase map and (b) the distribution of IQ index for body-centered-cubic phase. In (a), black areas show porosity; BD, RD, and SD are building direction, rolling direction, and the laser scanning direction, respectively.

grained and fine-grained ones. The coarse-grained component was comprised of columnar-shaped grains, which tended to align with the building direction and exhibited relatively bright IQ contrast (i.e., low stored energy). From the above characteristics, it was highly likely that this microstructural constituent was δ-ferrite. On the other hand, the fine-grained BCC component was characterized by a lath-shaped morphology and relatively dark IQ contrast (i.e., high stored energy). Hence, it was presumably α-martensite. The FCC constituent was obviously the austenitic phase. Therefore, in accordance with some literature data [11–13], the microstructure produced in the present study included three different phases, i.e., δ-ferrite, austenite, and martensite.

While the EBSD identification of austenite was relatively easy (Fig. 1a), the reliable discrimination between δ-ferrite and martensite was challenging. This problem arises from the relatively small difference in crystallography between the ferrite and martensite, which is difficult to resolve by EBSD.

To overcome this difficulty, a number of approaches have been elaborated recently [27–32]. These are based on the assumption that the energy stored within the ferrite and martensitic phases should be essentially different. Hence, the related EBSD characteristics (typically the IQ index) should exhibit a bimodal distribution. These approaches virtually imply the determination of a threshold magnitude, which delimitates two phases.

The IQ distributions derived from BCC constituents in the present study are shown in Fig. 1b and supplementary Fig. S5. In all cases, the distributions exhibited three distinct peaks. For simplicity, the borderlines between the peaks were indicated by the vertical dotted lines. Based on the revealed IQ thresholds, EBSD maps were partitioned into three microstructural components, as shown in Fig. 2 and supplementary Figs. S6 and S7. It was found that the data points with the lowest IQ index (e.g., the left peak in Fig. 1b) represented residual porosity (compare Fig. 2a and 1a). On the other hand, the central IQ peak (Fig. 1b) was associated with the fine-grained microstructure (compare Fig. 2b and 1a), thus presumably reflecting the martensitic phase. Finally, EBSD data with the highest IQ index were related to coarse columnar-shaped grains (compare Figs. 2c and 1a), i.e., δ-ferrite. Therefore, good agreement between the IQ distribution and phase structure was found in all cases. This suggests the feasibility of the employed approach for microstructure partitioning in the studied case.

Using this technique, the variations of the phase volume fractions along the building direction were examined (Table 2). In the bottom and central parts of the manufactured sample, the phase content was found

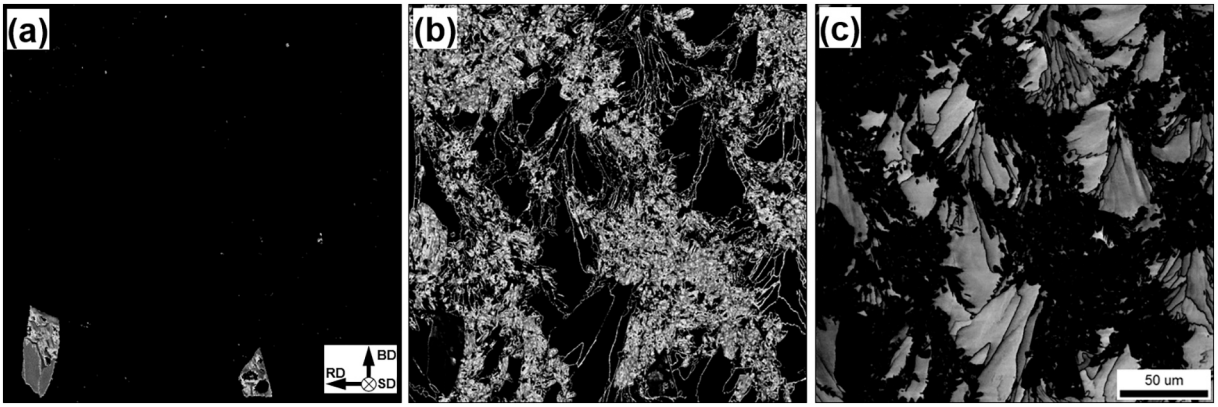

Fig. 2. Microstructure partitioning of EBSD map shown in Fig. 1a: (a) porosity, (b) α-martensite, and (c) δ-ferrite. In (a), RD, BD, and SD are rolling direction, building direction, and scanning direction, respectively.

Table 2
Variation of the phase volume fraction along building direction.

Location	Volume fraction, %			
	Porosity	δ-ferrite	austenite	α-martensite
Bottom	0.5	37.4	18.9	43.2
Center	0.6	38.8	17.6	43.0
Top	0.4	26.0	18.3	55.3

Note: The abrupt changes in the phase volume fraction are highlighted in gray.

to be nearly the same. In the top part, however, the martensite content increased at the expense of δ-ferrite (Table 2, highlighted in gray). The possible origin of this effect is discussed in Section 3.4.

Moreover, the phase partitioning provided an opportunity for detailed microstructural analysis in each particular phase. In turn, this allowed tracking of microstructural evolution that occurred during solidification and subsequent cooling of manufactured material. In the following three sections, these microstructural changes are considered in some detail.

3.2. Delta-ferrite

The presence of a significant volume fraction of δ-ferrite in the LPBF-induced microstructure (≈40% in Table 2) agrees with a number of published data [10–15]. Considering the high-temperature nature of this phase, its preservation at ambient conditions suggests an extremely high cooling rate. This is consistent with a typical magnitude of the cooling rate in excess of 10^6 K/s, which is typically attributed to LPBF [1].

Of particular interest was the observation that the δ-ferrite was not distributed uniformly throughout the microstructure but tended to cluster in local areas (Figs. 1a and 2c). These areas presumably reflected the former local molten pools produced during laser pulsing. Remarkably, the typical depth of such pools exceeded the average thickness of the powder layer (~70 μm vs 30 μm). This suggests that the manufactured material experienced at least two melting-to-solidification cycles during LPBF.

It is worth noticing that δ-ferrite was characterized by a relatively broad grain size distribution (Fig. 3a). Despite the typical grain size ranging from 20 to 30 μm (Fig. 3a), the manufactured material contained a significant portion of 1-μm grains (Figs. 3a and 2c). Given the fact that the fine grains were typically observed outside the ferrite clusters (Fig. 2c), they likely originated from the incomplete ferrite-to-austenite transformation.

In accordance with expectations, δ-ferrite exhibited a distinct {*hkl*}⟨100⟩ fiber texture (Fig. 3b, supplementary Fig. S8), thus suggesting the epitaxial nucleation mechanism [20,21]. Remarkably, crystallographic orientations of δ-ferrite tended to align with two external directions, viz. the laser scanning direction and the building direction. The two-component texture suggested the complex character of the thermal field generated during LPBF. The predominance of the <100>//SD component suggested that the heat transfer along the laser scanning direction was dominant.

Surprisingly, misorientation distribution in δ-ferrite was characterized by the crystallographic preference of 30° ⟨111⟩ and 60° < 111> boundaries (Fig. 4 and supplementary Figs. S9 and S10). Moreover, rotation axes of low-angle boundaries were found to cluster near the <110> pole (Fig. 4b and supplementary Figs. S9b and 10b). In order to access the possible effect of crystallographic texture on these effects, the texture-derived misorientation distribution was calculated. To this end, all possible misorientations between the sampled pixels were calculated, without considering any spatial correlation between them. However, no relation between the measured and calculated spectra was found (Fig. 4b). Hence, the unusual misorientation distribution in δ-ferrite was not associated with texture. Therefore, this issue warrants further study.

3.3. Austenite

The volume fraction of austenite in the manufactured material was measured to be ≈20% (Table 2). In contrast to δ-ferrite, the austenitic phase was distributed more or less homogeneously throughout the LPBF-induced microstructure, at least at mm-scale (Fig. 1a). Within the ferrite domains, however, austenite was typically associated with the ferrite grain boundaries (Fig. 5a). It was likely, therefore, that the δ-ferrite → austenite transformation was dominated by the grain-boundary nucleation. On the other hand, according to ThermoCalc predictions, a significant portion of austenite crystallized directly from the liquid phase (supplementary Fig. S1a).

To examine a possible orientation relationship between the austenite and δ-ferrite, a series of local crystallographic measurements were conducted. A typical example is shown in Figs. 5b and c. It was found that the grain-boundary austenite was crystallographically related to both adjacent ferrite grains (Figs. 5b and c). Furthermore, the orientation relationship was typically close to the Nishiyama-Wasserman (N-W), i.e., $\{110\}_\delta//\{111\}_\gamma$, $<110>_\delta//\langle 112\rangle_\gamma$ (Fig. 5c) rather than the Kurdjumov-Sachs (K-S), i.e., $\{110\}_\delta//\{111\}_\gamma$, $\langle 111\rangle_\delta//\langle 110\rangle_\gamma$ (supplementary Fig. S11).

To avoid the limited statistics of local measurements, the orientation relationship between the phases was also studied on an mm-scale, by comparing crystallographic textures in δ-ferrite and austenite (Fig. 6 and supplementary Figs. S12 and S13). These observations also showed that the N-W relationship (Fig. 6a) provided a better fit between the crystallographic orientations of the two phases than the K-S one (Fig. 6b).

As expected, the austenitic phase had a relatively fine-grained structure (Fig. 7a). Moreover, no significant variation in the grain size along the building direction was found (Fig. 7a).

The crystallographic texture in austenite was relatively weak. Specifically, the peak intensity in the inverse pole figures only slightly exceeded 1.3 times random (Fig. 7b and supplementary Fig. S14). Nevertheless, the preferential alignment of <110> axis along both the laser scanning direction and the building direction was found. The formation of <110> – fiber texture in the austenitic phase during LPBF of 17–4 PH martensitic steel has been reported by Murr et al. [2,16] and Wang et al. [19]. Moreover, the development of ⟨001⟩//SD orientation was observed in the present study (Fig. 7b). In austenitic steels, crystallographic preference of this orientation is usually associated with solidification texture [33,34]. Hence, this textural component may result from the direct solidification of austenite from molten material.

Misorientation distribution in the austenitic phase was characterized by an increased proportion of 60° < 111> and ≈40° ⟨110⟩ misorientations (Fig. 8, supplementary Figs. S15 and S16). In cubic metals (including austenite), crystallographic preference of such boundaries is usually associated with extensive twinning. Considering the strain-less nature of LPBF treatment, the twinning was likely attributable to the growth faulting that occurs during grain-boundary migration. Interestingly, the twins in the present study were typically linked to *phase* boundaries rather than to the grain boundaries (supplementary Fig. S17).

Thus, the texture revealed in austenite likely resulted from three mechanisms: (i) the reorientation of the {*hkl*}<100 > solidification texture in δ-ferrite due to the N-W orientation relationship between the phases, (ii) annealing twinning, and (iii) direct solidification of austenite

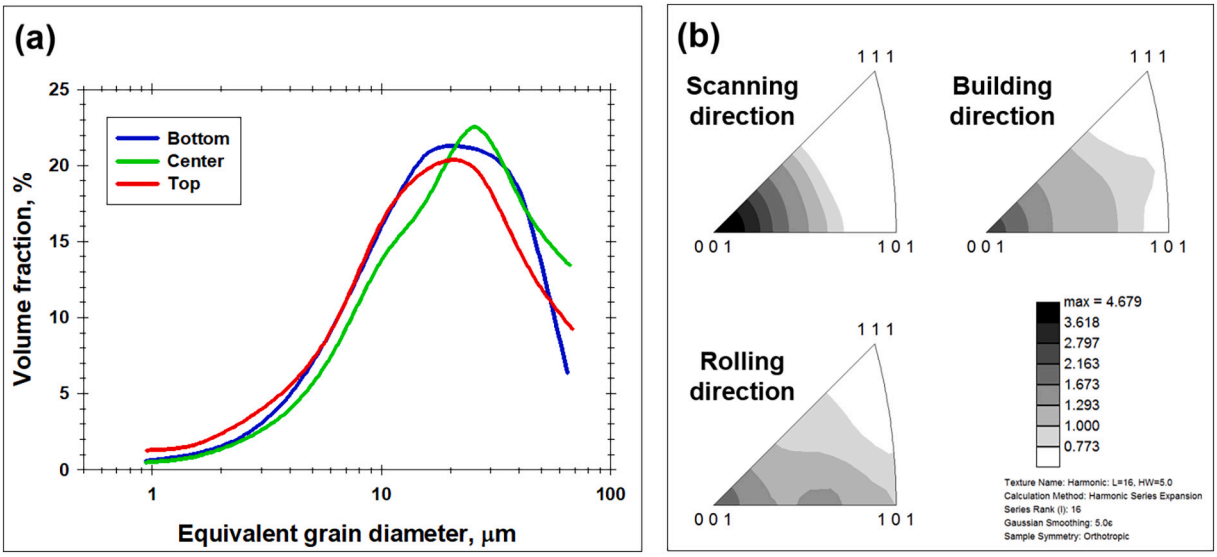

Fig. 3. (a) Grain-size distributions and (b) typical crystallographic texture in δ-ferrite.

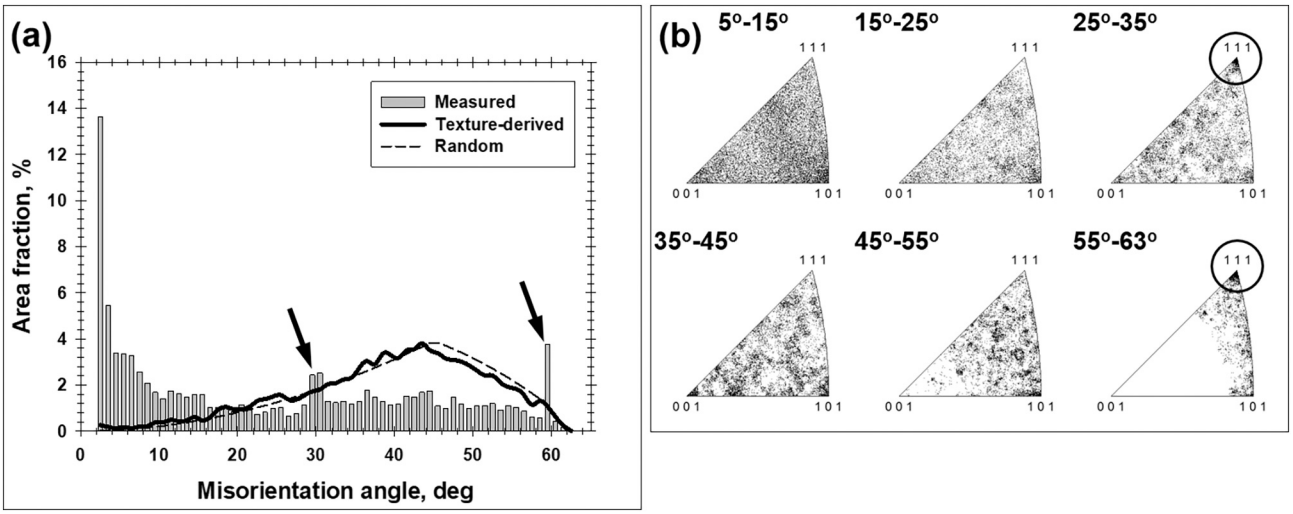

Fig. 4. Typical misorientation distributions derived from δ-ferrite: (a) misorientation-angle distribution and (b) misorientation-axis distribution.

from the liquid phase. Normally, two former processes involve multiple crystallographic variants and thus should reduce texture intensity. This was indeed observed in the present study (Fig. 7b and supplementary Fig. S14).

The grain-boundary nucleation mechanism as well as abundant annealing twinning that occurred during migration of phase boundaries suggested that the δ-ferrite → austenite transformation was governed by a diffusion mechanism.

3.4. Martensite

The volume fraction of martensite was measured to be ≈40% (Table 2). Remarkably, this phase was typically arranged in-between the ferrite domains (compare Fig. 1a and 2b), i.e., virtually near the outer borders of the former molten pools. These areas should be most influenced by thermal cycling, which is intrinsic to the LPBF process. Hence, the cooling rate there may be sufficiently low for the realization of the normal phase transformation sequence, i.e., δ-ferrite → austenite → α-martensite.

It is believed that the cooling rate should decrease with distance from the backing plate. This effect should promote decomposition of δ-ferrite and thus may explain the observed variation of the ferrite/martensite ratio along the building direction (Table 2).

Local orientation measurements revealed that the crystallographic relationship between the martensite and austenite can be described in terms of both K-S and N-W orientation relations (Fig. 9). On the other hand, the comparison of appropriate texture data suggested the prevalence of the N-W one (Fig. 10 and supplementary Figs. S18 and S19).

As expected, the martensite exhibited lath-shaped morphology (Fig. 9b) and relatively fine grain size (Fig. 11a). On the other hand, no evidence of classical hierarchical transformation microstructure (including prior-austenite grains, martensite packets, and martensite blocks) was found. This was presumably due to the fine-grained nature of the austenitic phase in the studied case (Fig. 7a).

The martensite exhibited <100> – fiber texture along both the laser-scanning and building directions (Fig. 11b and supplementary Fig. S20). This was broadly similar to the original solidification texture in δ-ferrite (Fig. 3b). Hence, the δ-ferrite → austenite → α-martensite transformation sequence virtually reproduced the original crystallographic orientations, though the texture intensity in martensite was ~2.5 times lower than in δ-ferrite (compare Figs. 3b and 11b). Moreover, the martensitic phase was also characterized by an additional <111>//SD

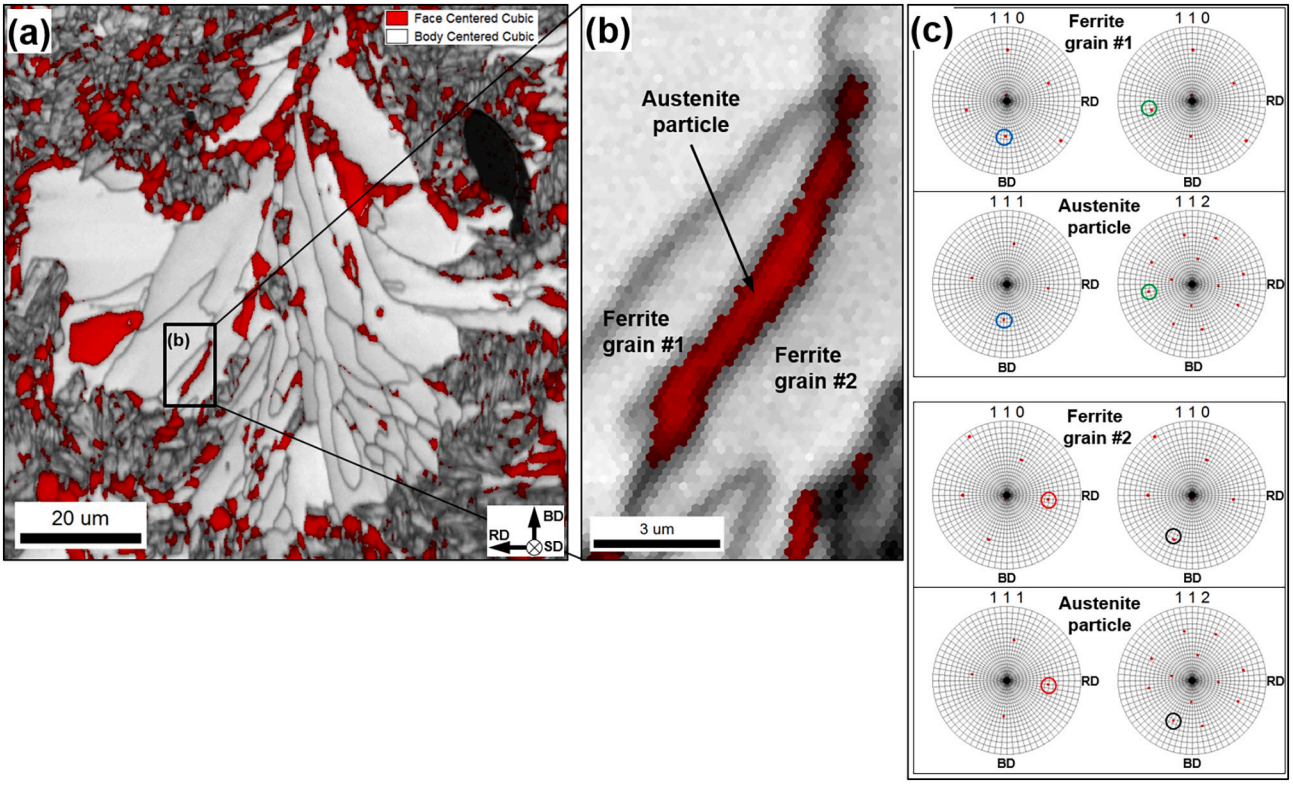

Fig. 5. (a) High-resolution EBSD IQ map with overlaid phase map, (b) the selected area shown at higher magnification and illustrating grain-boundary austenite, and (c) pole figures exemplifying the local Nushiyama-Wasserman orientation relationship between δ-ferrite and grain-boundary austenite. In (c), the closest related orientations in δ-ferrite and the austenite are circled. BD, RD, and SD are building direction, rolling direction, and the laser scanning direction, respectively.

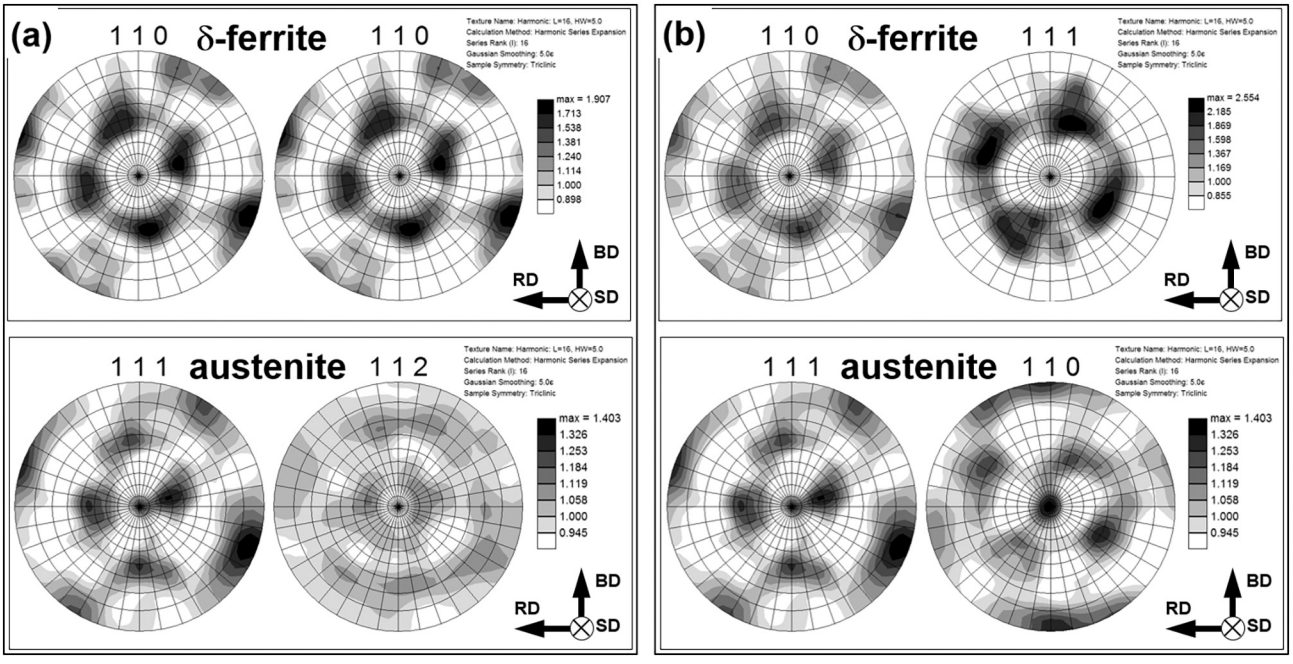

Fig. 6. Examination of orientation relationship between δ-ferrite and austenite in mm-scale: (a) Nushiyama-Wasserman (N-W) orientation relationship and (b) Kurdjumov-Sachs (K-S) orientation relationship. BD, RD, and SD are building direction, rolling direction, and the laser scanning direction, respectively.

component (Fig. 11b and supplementary Fig. S20). This observation agreed with the recent finding by Wang et al. [19]. From the broad perspective, the two-component texture in martensite is consistent with that in austenite (compare Figs. 11b and 7b). Hence, the texture in martensite presumably originated from the orientation relationship between the phases. However, the details of this process are unclear and thus warrant further study.

Unsurprisingly, misorientation-angle distribution in martensite was characterized by pronounced low-angle maxima and a broad peak near 50-60^{o} (Fig. 12a). The broadly similar distributions are typically

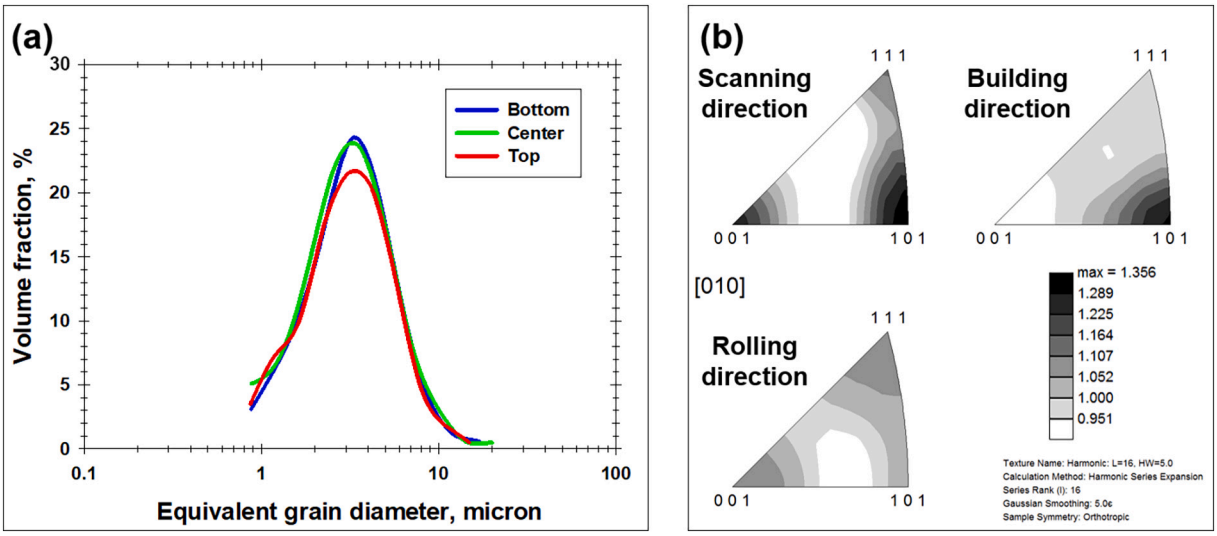

Fig. 7. (a) Grain-size distributions and (b) typical crystallographic texture derived from austenite.

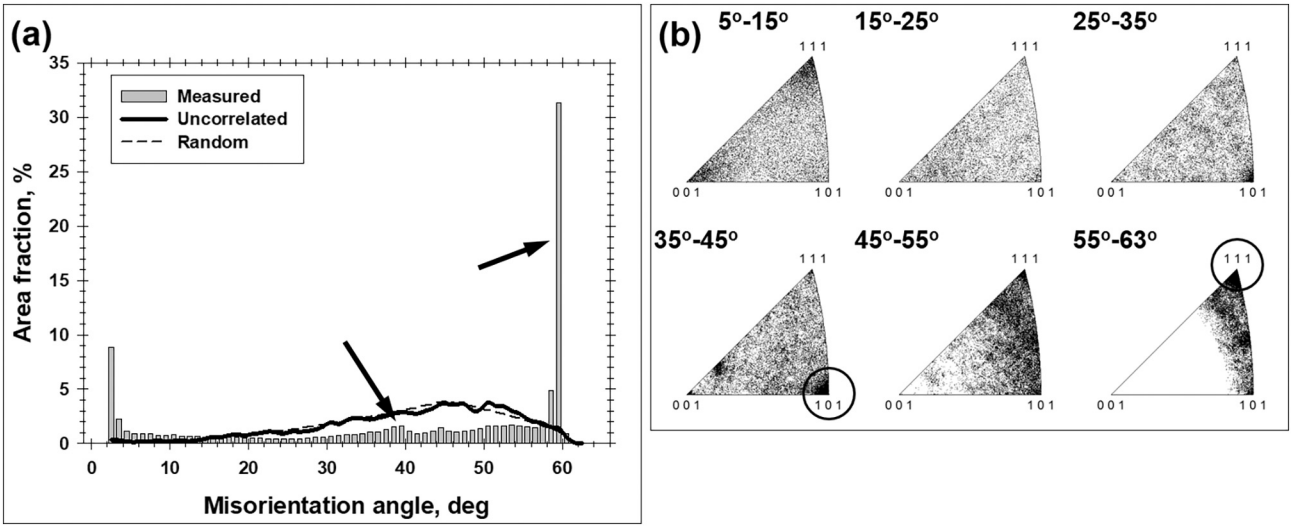

Fig. 8. Typical misorientation distributions derived from austenite: (a) misorientation-angle distribution and (b) misorientation-axis distribution. Note: Arrows in (a) and selected areas in (b) illustrate crystallographic preference of Σ3 and Σ9 misorientations.

observed in martensitic structures irrespective of the particular orientation relationship with the austenitic phase (i.e., K-S vs. N-W) [e.g. 35]. In order to clarify the orientation relation, the measured misorientation axes (Fig. 12b and supplementary Fig. S21) were compared with those predicted for K-S, N-W, and mixed[2] (K-S + N-W) relationships (Fig. 12c). This comparison showed that the mixed relationship provides the best fit with experimental data.

It is worth noting that the measured misorientation distribution in martensite was also characterized by an increased proportion of 30^{o} < 111> boundaries (Figs. 12a and b). This misorientation is not consistent with that expected between crystallographic variants of martensitic transformation (at least, assuming K-S and N-W orientation relationships). Therefore, its origin is unclear and requires clarification.

3.5. Elemental distribution and second-phase particles

In order to get a deeper insight into the microstructure of the produced material, the spatial distribution of alloying elements was mapped using a combined EBSD and EDS technique, as shown in Fig. 13a and b-h, respectively. A significant fraction of comparatively-coarse (~10 μm) silicon- and manganese-rich particles was found (Figs. 13b-c). According to ThermoCalc predictions, these particles presumably represented G-phase, which precipitated at temperatures as low as 350 °C (supplementary Fig. S1b). Indeed, these particles were typically observed in the fine-grained (i.e., martensite-rich) areas (compare Figs. 13b-c with 13a). The formation of such particles during LPBF of 17–4 PH steel has been reported by Sun et al. [11,23]. However, the precipitation mechanism of these particles as well as their influence on microstructural evolution is not clear and warrants further study.

On the other hand, chromium, niobium, copper, and nickel were evenly distributed throughout the material, and no essential elemental partitioning between δ-ferrite, austenite, and α-martensite was found (compare Figs. 13e-h and 13a). Alnajjar et al. [20] have attributed this effect to the extremely high cooling rate during LPBF, which hampered

[2] The mixed orientation relationship assumes that the adjoining martensite variants were produced according to both K-S and N-W relations [35].

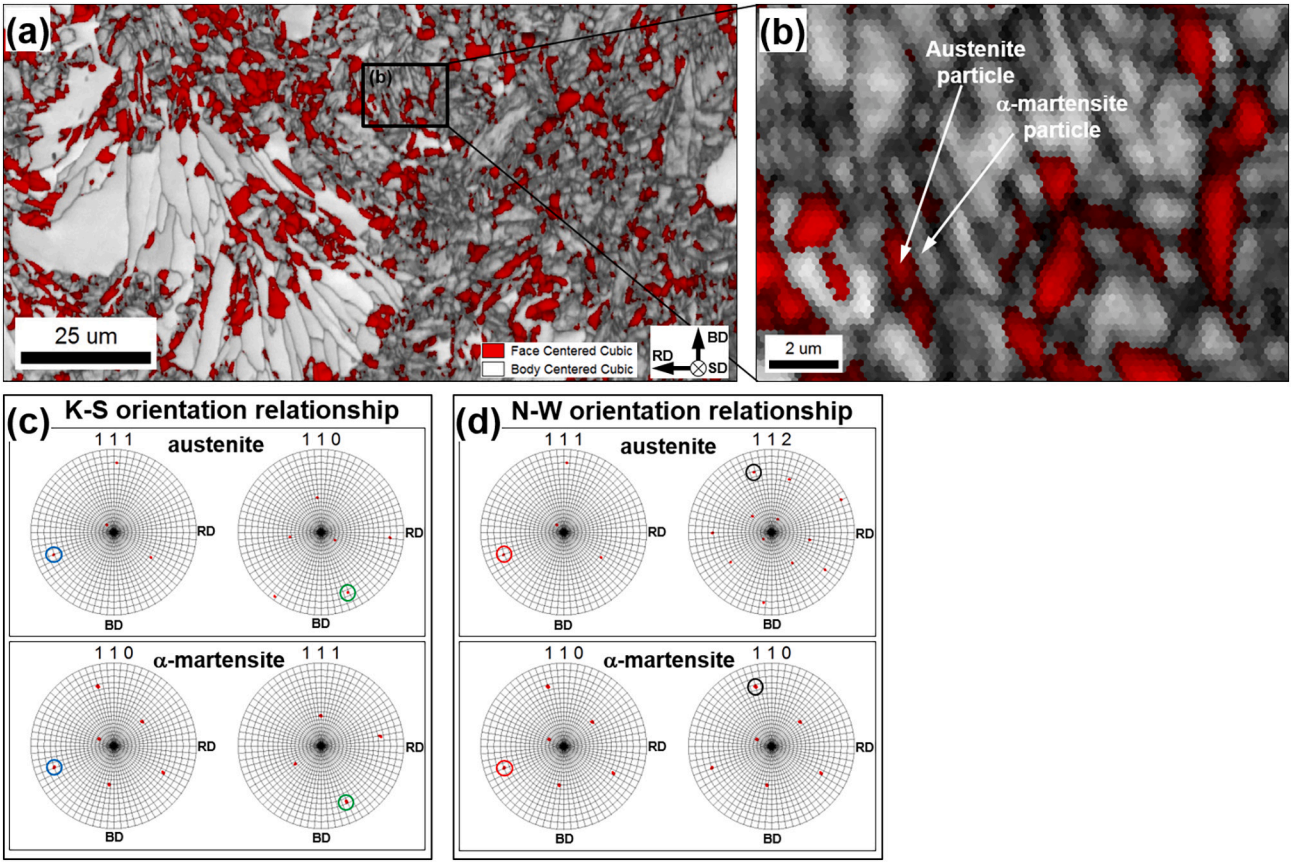

Fig. 9. (a) High-resolution EBSD IQ map with overlaid phase map, (b) the selected area shown at higher magnification and illustrating the adjoining austenite and α-martensite phases, (c) pole figures showing the local Kurdjumov-Sachs (K-S) orientation relationship between the austenite and martensite, and (d) pole figures showing the local Nushiyama-Wasserman (N-W) orientation relationship between the austenite and martensite. In (c) and (d), the closest related orientations in the austenite and the martensite are circled. BD, RD, and SD are building direction, rolling direction, and the laser scanning direction, respectively.

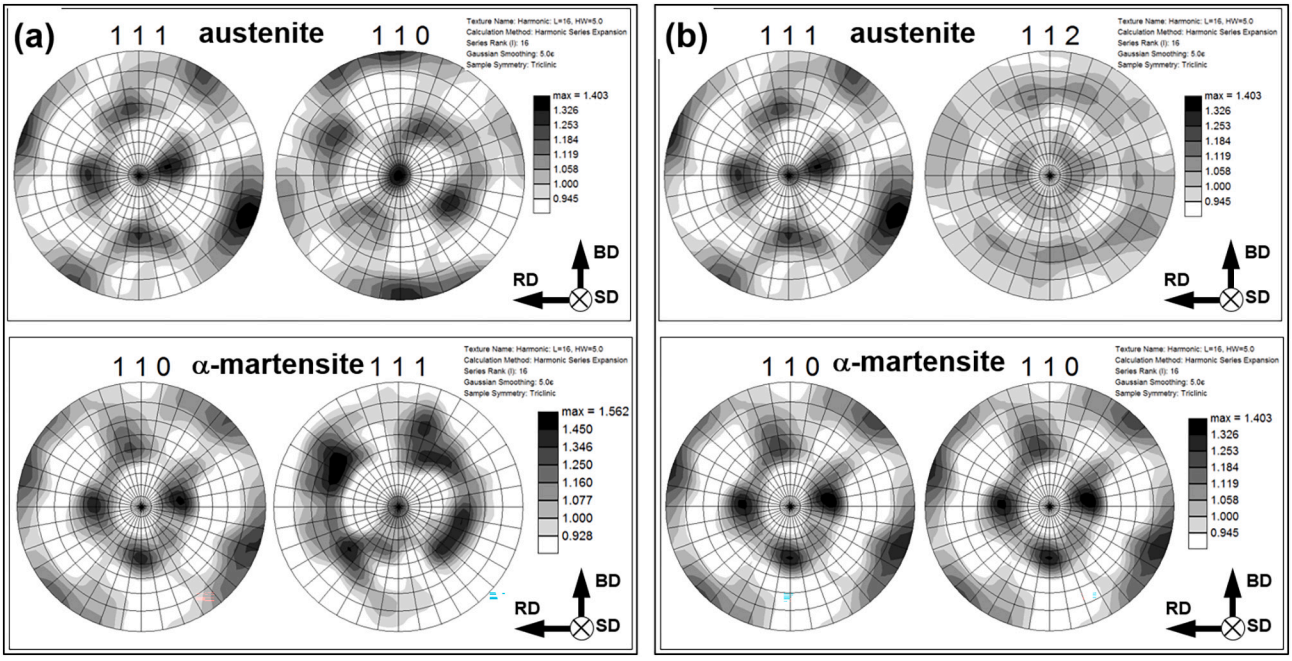

Fig. 10. Examination of orientation relationship between austenite and α-martensite in mm-scale: (a) Kurdjumov-Sachs (K-S) orientation relationship and (b) Nushiyama-Wasserman (N-W) orientation relationship. BD, RD, and SD are building direction, rolling direction, and the laser scanning direction, respectively.

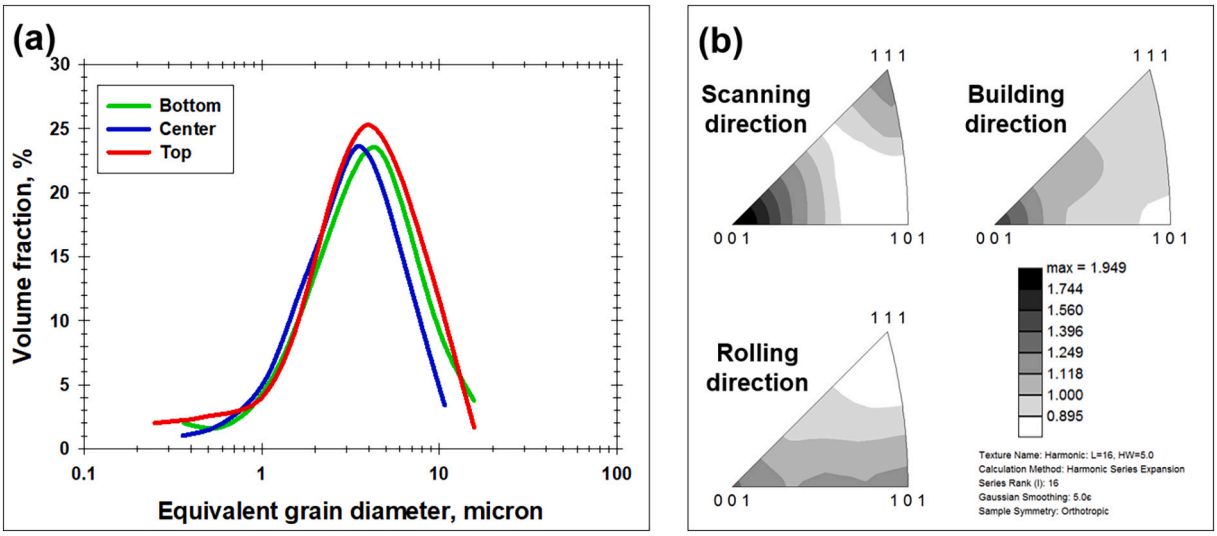

Fig. 11. (a) Grain-size distributions and (b) typical crystallographic texture derived from α-martensite.

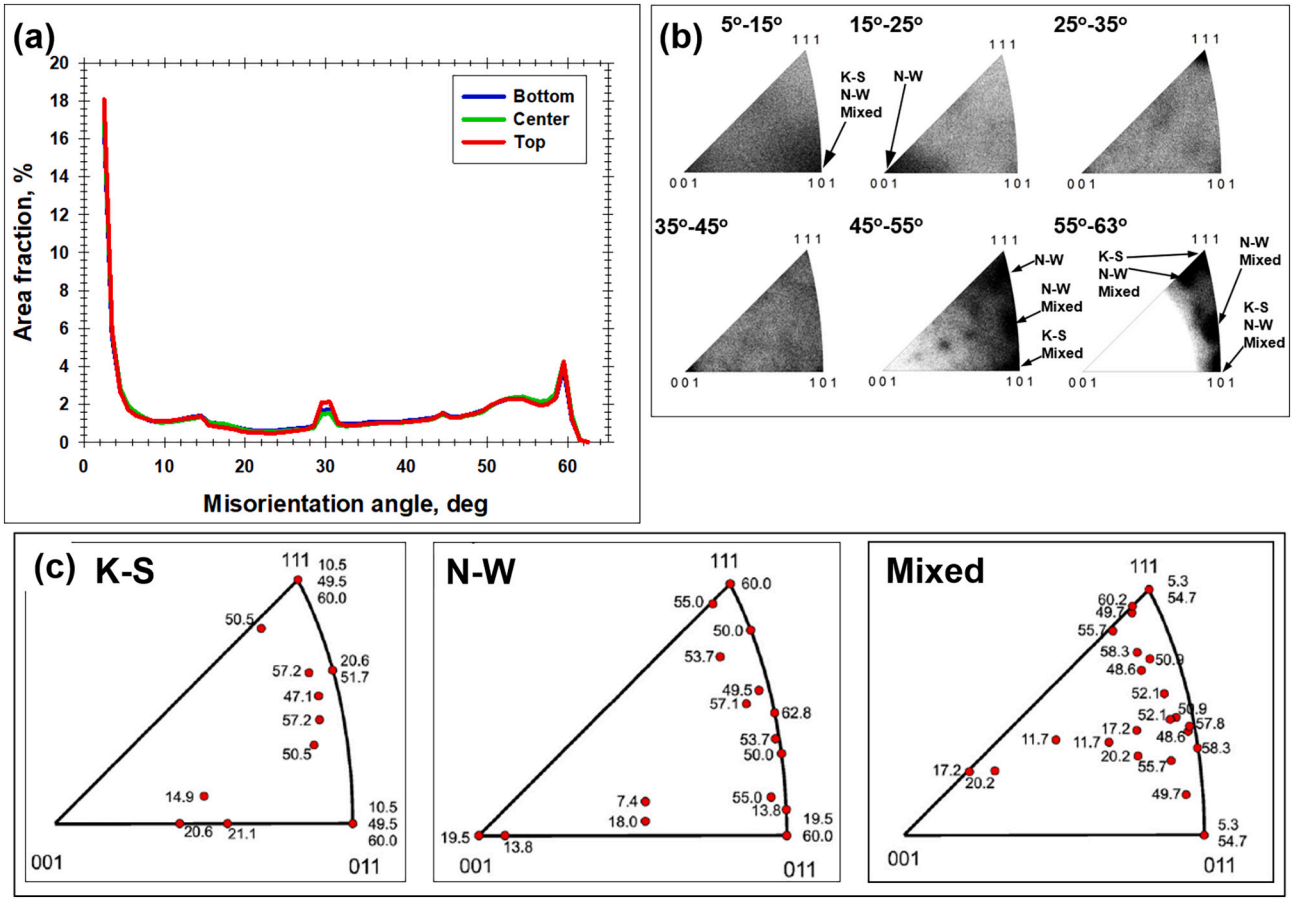

Fig. 12. (a) Misorientation-angle distributions, (b) typical misorientation-axis distribution, and (c) distributions of misorientation axes of inter-variant boundaries between martensite variants expected for Kurdjumov-Sachs (K-S), Nushiyama-Wasserman (N-W), and mixed orientation relationships (after Sonderegger et al. [35]). In (b), arrows show misorientation axes expected for particular orientation relationship. In (c), numbers show misorientation angles of particular inter-variant boundaries.

the gross redistribution of the alloying elements between the phases. It is important to emphasize that the above observation was not consistent with the diffusion-derived mechanism of the δ-ferrite → austenite transformation (as suggested in Section 3.3). Therefore, this issue requires an additional investigation.

It is highly likely that manufactured material also contained the fine dispersoids, which were beyond the resolution limit of the applied EDS technique. Specifically, the formation of nano-scale oxides has been reported by Sun et al. [11,23]. However, examination of such precipitations was outside the scope of the present study.

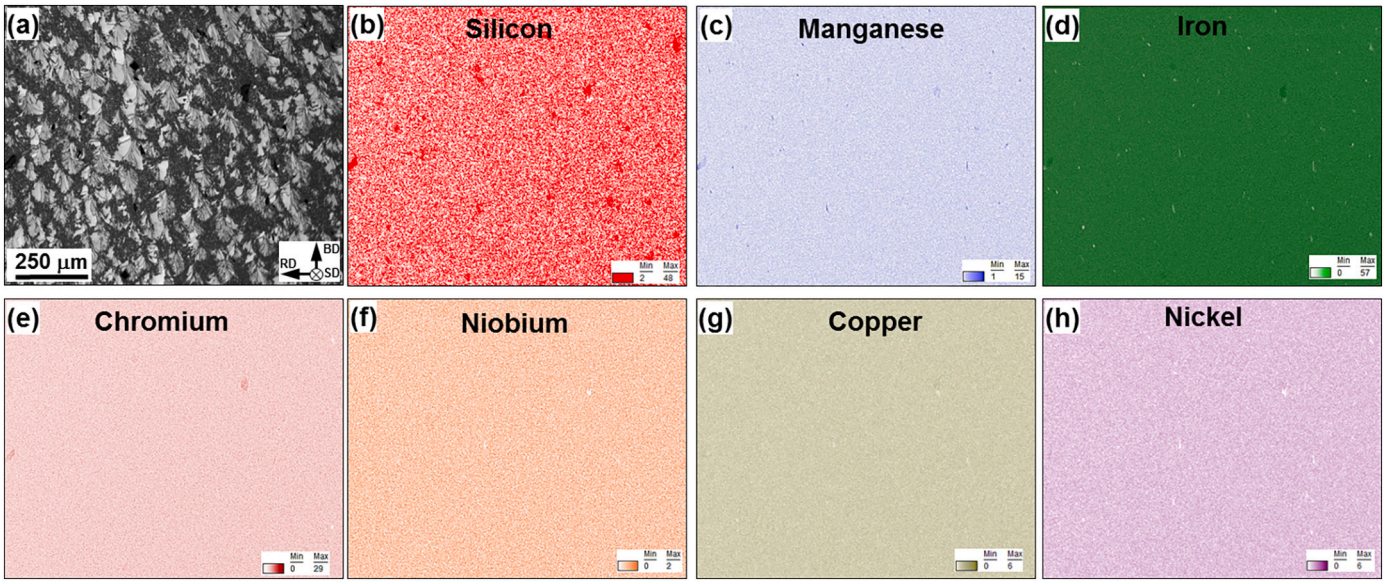

Fig. 13. (a) Low-resolution EBSD IQ map, and a series of EDS maps taken from the same area and showing spatial distribution of particular elements: (b) silicon, (c) manganese, (d) iron, (e) chromium, (f) niobium, (g) copper, and (h) nickel. Note: The scale bar and reference frame for all maps are indicated in the bottom part of (a); BD, RD and SD are building direction, rolling direction, and the laser scanning direction, respectively.

4. Summary

This work was undertaken in order to explore crystallographic aspects of the 17–4 PH steel produced by the LPBF technique. Particular emphasizes was given to the examination of the orientation relationships between δ-ferrite, austenite, and martensite, crystallographic texture, and misorientation distributions in all these phases. Based on experimental observations, the following pattern of microstructural evolution during LPBF was suggested.

(1) The microstructural evolution was critically influenced by the particular location of material within the local molten pool. In the central part of the pool, this process was typically confined by the crystallization of δ-ferrite from the liquid phase. Presumably due to the extremely high cooling rate inherent to LPBF, the following decomposition of this phase was inhibited and thus it survived down to ambient temperature. At the outer edge of the molten pool, however, the normal δ-ferrite → austenite → martensite phase transformation sequence was realized. The sufficiently low cooling rate in this area was likely associated with thermal cycling, which is also intrinsic to LPBF. Therefore, the manufactured material exhibited a bimodal microstructure consisting of domains of the coarse δ-ferrite grains surrounded by finer-grained austenite and martensite.

(2) The nucleation and growth of δ-ferrite was governed by an epitaxial mechanism, which gave rise to the solidification <100> – fiber texture in this phase. Due to the complex nature of the thermal field within the molten pool, the texture included two components, which were aligned with both the laser scanning direction and the building direction.

(3) The δ-ferrite → austenite phase transformation was driven by a diffusion mechanism. Specifically, the austenite phase preferentially nucleated at the ferrite grain boundaries, and the migration of phase boundaries promoted extensive annealing twinning. Importantly, the grain-boundary austenite was related to both adjacent ferrite grains via the N-W orientation relationship. The multiple crystallographic variants associated with the phase transformation and annealing twinning resulted in a comparatively weak crystallographic texture in austenite.

(4) The austenite → martensite phase transformation was governed by the mixed (K-S + N-W) orientation relationship. Due to the fine-grained nature of austenite, no classical hierarchical microstructure (including prior-austenite grains, martensite packets, and martensite blocks) was found in the martensitic phase. The nearly-random texture in martensite suggested no essential variant selection during the phase transformation.

Data availability

The raw/processed data required to reproduce these findings cannot be shared at this time as the data also forms part of an ongoing study.

Declaration of Competing Interest

The authors declare that they have no known competing financial interests or personal relationships that could have appeared to influence the work reported in this paper.

Data availability

Data will be made available on request.

Acknowledgment

This work was performed using the equipment of the Joint Research Center “Technology and Materials” at Belgorod National Research University (financial support from the Ministry of science and higher education of the Russian Federation under the agreement No. 075-15-2021-690, the unique project identifier RF 2296.61321X0030). The authors are grateful to Alexander Kalinenko for help with experiments.

Appendix A. Supplementary data

Supplementary data to this article can be found online at https://doi.org/10.1016/j.matchar.2022.112405.

References

[1] D.D. Gu, W. Meiners, K. Wissenbach, R. Poprawe, Laser additive manufacturing of metallic components: materials, processes and mechanisms, Int. Mater. Rev. 57 (2012) 133–164, https://doi.org/10.1179/1743280411Y.0000000014.

[2] L.E. Murr, S.M. Gaytan, D.A. Ramirez, E. Martinez, J. Hernandez, K.N. Amato, P. W. Shindo, F.R. Medina, R.B. Wicker, Metal fabrication by additive manufacturing using laser and electron beam melting technologies, J. Mater. Sci. Technol. 28 (2012) 1–14, https://doi.org/10.1016/S1005-0302(12)60016-4.

[3] A. Yadollahi, N. Shamsaei, S.M. Thompson, A. Elwany, L. Bian, Effects of building orientation and heat treatment on fatigue behavior of selective laser melted 17-4 PH stainless steel, Int. J. Fatigue 94 (2017) 218–235, https://doi.org/10.1016/j.ijfatigue.2016.03.014.

[4] H.K. Rafi, D. Pal, N. Patil, T.L. Starr, B.E. Stucker, Microstructure and mechanical behavior of 17-4 precipitation hardenable steel processed by selective laser melting, J. Mater. Eng. Perform. 23 (2014) 4421–4428, https://doi.org/10.1007/s11665-014-1226-y.

[5] T. LeBrun, T. Nakamoto, K. Horikawa, H. Kobayashi, Effect of retained austenite on subsequent thermal processing and resultant mechanical properties of selective laser melted 17–4 PH stainless steel, Mater. Des. 81 (2015) 44–53, https://doi.org/10.1016/j.matdes.2015.05.026.

[6] R. Rashid, S.H. Masood, D. Ruan, S. Palanisamy, R.A. Rahman Rashid, M. Brandt, Effect of scan strategy on density and metallurgical properties of 17-4PH parts printed by selective laser melting (SLM), J. Mater. Process. Technol. 249 (2017) 502–511, https://doi.org/10.1016/j.jmatprotec.2017.06.023.

[7] S. Pasebani, M. Ghayoor, S. Badwe, H. Irrinki, S.V. Atre, Effects of atomizing media and post processing on mechanical properties of 17-4 PH stainless steel manufactured via selective laser melting, Add. Manuf. 22 (2018) 127–137, https://doi.org/10.1016/j.addma.2018.05.011.

[8] T.-H. Hsu, Y.-J. Chang, C.-Y. Huang, H.-W. Yen, C.-P. Chen, K.-K. Jen, A.-C. Yeh, Microstructure and property of a selective laser melting process induced oxide dispersion strengthened 17-4 PH stainless steel, J. Alloys Compd. 803 (2019) 30–41, https://doi.org/10.1016/j.jallcom.2019.06.289.

[9] X. Wang, Y. Liu, T. Shi, Y. Wang, Strain rate dependence of mechanical property in a selective laser melted 17–4 PH stainless steel with different states, Mater. Sci. Eng. A 792 (2020) 139776, https://doi.org/10.1016/j.msea.2020.139776.

[10] M. Akita, Y. Uematsu, T. Kakiuchi, M. Nakajima, R. Kawaguchi, Defect-dominated fatigue behavior in type 630 stainless steel fabricated by selective laser melting, Mater. Sci. Eng. A 666 (2016) 19–26, https://doi.org/10.1016/j.msea.2016.04.042.

[11] Y. Sun, R.J. Hebert, M. Aindow, Effect of heat treatments on microstructural evolution of additively manufactured and wrought 17-4PH stainless steel, Mater. Des. 156 (2018) 429–440, https://doi.org/10.1016/j.matdes.2018.07.015.

[12] S. Vunnam, A. Saboo, C. Sudbrack, T.L. Starr, Effect of powder chemical composition on the as-built microstructure of 17-4 PH stainless steel processed by selective laser melting, Addit. Manuf. 30 (2019) 100876, https://doi.org/10.1016/j.addma.2019.100876.

[13] P. Leo, S. D'Ostuni, P. Perulli, M.A.C. Sastre, A.I. Fernández-Abia, J. Barreiro, Analysis of microstructure and defects in 17-4 PH stainless steel sample manufactured by selective laser melting, Proc. Manuf. 41 (2019) 66–73, https://doi.org/10.1016/j.promfg.2019.07.030.

[14] M. Alnajjar, F. Christien, V. Barnier, C. Bosch, K. Wolski, A.D. Fortes, M. Telling, Influence of microstructure and manganese sulfides on corrosion resistance of selective laser melted 17-4 PH stainless steel in acidic chloride medium, Corros. Sci. 168 (2020) 108585, https://doi.org/10.1016/j.corsci.2020.108585.

[15] M. Alnajjar, F. Christien, C. Bosch, K. Wolski, A comparative study of microstructure and hydrogen embrittlement of selective laser melted and wrought 17–4 PH stainless steel, Mater. Sci. Eng. A 785 (2020) 139363, https://doi.org/10.1016/j.msea.2020.139363.

[16] L.E. Murr, E. Martinez, J. Hernandez, S. Collins, K.N. Amato, S.M. Gaytan, P. W. Shindo, Microstructures and properties of 17-4 PH stainless steel fabricated by selective laser melting, J. Mater. Res. Technol. 1 (2012) 167–177, https://doi.org/10.1016/S2238-7854(12)70029-7.

[17] R. Shabadi, M. Ionescu, M. Jeandin, C. Richard, T. Chandra, Water atomized 17-4 PH stainless steel powder as a cheaper alternative powder feedstock for selective laser melting, Mater. Sci. Forum 941 (2018) 698–703, https://doi.org/10.4028/www.scientific.net/MSF.941.698.

[18] T.-H. Hsu, P.-C. Huang, M.-Y. Lee, K.-C. Chang, C.-C. Lee, M.-Y. Li, C.-P. Chen, K.-K. Jen, A.-C. Yeh, Effect of processing parameters on the fractions of martensite in 17-4 PH stainless steel fabricated by selective laser melting, J. Alloys Compd. 859 (2021) 157758, https://doi.org/10.1016/j.jallcom.2020.157758.

[19] H.R. Lashgari, Y. Xue, C. Onggowarsito, C. Kong, S. Li, Microstructure, tribological properties and corrosion behaviour of additively manufactured 17–4PH stainless steel: effects of scanning pattern, build orientation, and single vs. double scan, Mater. Today Comm. 25 (2020) 101535, https://doi.org/10.1016/j.mtcomm.2020.101535.

[20] M. Alnajjar, F. Christien, K. Wolski, C. Bosch, Evidence of austenite by-passing in a stainless steel obtained from laser melting additive manufacturing, Add. Manuf. 25 (2019) 187–195, https://doi.org/10.1016/j.addma.2018.11.004.

[21] L. Zai, C. Zhang, Y. Wang, W. Guo, D. Wellmann, X. Tong, Y. Tian, Laser powder bed fusion of precipitation-hardened martensitic stainless steels: a review, Metals 10 (2) (2020) 255–280, https://doi.org/10.3390/met10020255.

[22] L.E. Murr, E. Martinez, K.N. Amato, S.M. Gaytan, J. Hernandez, D.A. Ramirez, P. W. Shindo, F. Medina, R.B. Wicker, Fabrication of metal and alloy components by additive manufacturing: examples of 3D materials science, J. Mater. Res. Technol. 1 (2012) 42–54, https://doi.org/10.1016/S2238-7854(12)70009-1.

[23] Y. Sun, R.J. Hebert, M. Aindow, Non-metallic inclusions in 17-4PH stainless steel parts produced by selective laser melting, Mater. Des. 140 (2018) 153–162, https://doi.org/10.1016/j.matdes.2017.11.063.

[24] C. Rowolt, B. Milkereit, P. Andreazza, O. Kessler, Quantitative high temperature calorimetry on precipitation in steel and nickel alloys, Thermochim. Acta 677 (2019) 169–179, https://doi.org/10.1016/j.tca.2019.01.026.

[25] C. Rowolt, B. Milkereit, A. Springer, C. Kreyenschulte, O. Kessler, Dissolution and precipitation of copper-rich phases during heating and cooling of precipitation-hardening steel X5CrNiCuNb16-4 (17-4 PH), J. Mater. Sci. 55 (2020) 13244–13257, https://doi.org/10.1007/s10853-020-04880-4.

[26] F.J. Humphreys, Quantitative metallography by electron backscatter diffraction, J. Microsc. 195 (1999) 170–185, https://doi.org/10.1046/j.1365-2818.1999.00578.x.

[27] A.W. Wilson, J.D. Madison, G. Spanos, Determining phase volume fraction in steels by electron backscattered diffraction, Scr. Mater. 45 (2001) 1335–1340, https://doi.org/10.1016/S1359-6462(01)01137-X.

[28] J. Wu, P.J. Wray, C.I. Garcia, M. Hua, A.J. Deardo, Image quality analysis: a new method of characterizing microstructures, ISIJ Int. 45 (2005) 254–262, https://doi.org/10.2355/isijinternational.45.254.

[29] M.M. Nowell, S.I. Wright, J.O. Carpenter, Differentiating ferrite and martensite in steel microstructures using electron backscatter diffraction, in: Proc. Materials Science and Technology Conference and Exhibition, 2009.

[30] M. Calcagnotto, D. Ponge, D. Raabe, Microstructure control during fabrication of ultrafine grained dual-phase steel: characterization and effect of intercritical annealing parameters, ISIJ Int. 52 (2012) 874–883, https://doi.org/10.2355/isijinternationl.52.874.

[31] J.-Y. Kang, S.-J. Park, M.-B. Moon, Phase analysis on dual-phase steel using bnd slope of electron backscatter diffraction pattern, Microsc. Microanal. 19 (2013) 13–16, https://doi.org/10.1017/S1431927613012233.

[32] T. Martinez Ostormujof, R.R.P. Purushottam Raj Purohit, S. Breumier, N. Gey, M. Salib, L. Germain, Deep learning for automated phase segmentation in EBSD maps. A case study in dual phase steel microstructures, Mater. Charact. 184 (2022) 111638, https://doi.org/10.1016/j.matchar.2021.111638.

[33] A. Hunter, M. Ferry, Phase formation during solidification of AISI 304 austenitic stainless steel, Scr. Mater. 46 (2002) 253–258, https://doi.org/10.1016/S1359-6462(01)01215-5.

[34] D. Raabe, Microstructure and crystallographic texture of strip-cast and hot-rolled austenitic stainless steel, Metall. Mater. Trans. A 26 (1995) 991–998, https://doi.org/10.1007/BF02649096.

[35] B. Sonderegger, S. Mitsche, H. Cerjak, Martensite laths in creep resistant martensitic 9–12% Cr steels — calculation and measurement of misorientations, Mater. Charact. 58 (2007) 874–882, https://doi.org/10.1016/j.matchar.2006.08.014.